Supplementary Information

Ru species decoration on hierarchical Nb_2O_{5-x} modulates product selectivity for CO_2 photoreduction

Yeqiang Zhai, Guimin Wang, Nan Wang, Yanqing Jiao*, Dongxu Wang, Haijing Yan, Yuxian Jiang, Aiping Wu, and Honggang Fu*

Key Laboratory of Functional Inorganic Material Chemistry, Ministry of Education of the People's Republic of China, National Center for International Research on Catalytic Technology, Heilongjiang University, Harbin 150080, China

*E-mail: fuhg@hlju.edu.cn; fuhg@vip.sina.com; jiaoyanqing@hlju.edu.cn; jiaoyq617@outlook.com

Experiment details

Materials and reagents

Niobium oxalate ($C_{10}H_5NbO_{20}\cdot xH_2O$), L-arginine ($C_6H_{14}N_4O_2$), $RuCl_3\cdot xH_2O$ and niobium oxide (Nb_2O_5) were purchased from Aladdin Reagent Co., Ltd. Citric acid and $NaBH_4$ were purchased from Tianjin Kemio Chemical Reagent Co., Ltd. Ethanol was obtained from Tianjin Fuyu Fine Chemical Co., Ltd. All purchased chemicals and reagents were of analytical grade and used without further purification.

Preparation of Nb_2O_{5-x}

1 mmol of $C_{10}H_5NbO_{20}\cdot xH_2O$ was dissolved in a mixture of 15 mL deionized water and 10 mL ethanol. The suspension was then heated to 60℃ under magnetic stirring for 20 min until a clear solution (solution A) was formed. Then, 0.25 mmol of L-arginine dissolved in 5 mL deionized water was added to solution A, followed by continued stirring for another 20 min. The resulting mixture was transferred into a 50 mL Teflon-lined autoclave and heated at 180 ℃ for 12 h, then allowed to cool naturally to room temperature. After repeated centrifugation and drying at 60 ℃, the product was collected and denoted as the NbO precursor. Finally, the NbO precursor was calcined in air at 350 ℃ for 3 h in a muffle furnace, with a heating rate of 10 ℃ min^{-1}. The resulting yellow solid was denoted as Nb_2O_{5-x}.

Preparation of Ov-Nb_2O_5

Similar to the synthesis of Nb_2O_{5-x}, 4 mmol of citric acid was used instead of arginine. The resulting yellow solid was denoted as Ov-Nb_2O_5.

Preparation of Ru-Nb_2O_{5-x}

Typically, 1 mL of $RuCl_3\cdot xH_2O$ (1 mg mL^{-1}) was dispersed into 20 mL of a solution containing Nb_2O_{5-x} (25 mg), and stirred for 20 min at room temperature. During the stirring process, 2 mL of $NaBH_4$ solution (0.1 M) was added, followed by continuous stirring for 1 h. The resulting sample was then washed with water and ethanol. After drying at 60 °C overnight, the final sample, denoted as Ru-Nb_2O_{5-x}, was obtained. The as-synthesized Ru-Nb_2O_{5-x} photocatalyst exhibited an actual Ru content of 1.02 wt%,

as determined by ICP–OES. Furthermore, adjusting the volume of $RuCl_3 \cdot xH_2O$ solution to 0.25, 0.5, and 2 mL, resulted in actual Ru contents of 0.33, 0.65, and 1.22 wt%, respectively.

Characterization

Powder X-ray diffraction (XRD) measurements were performed on a Bruker D8 Advanced diffractometer with nickel-filtered Cu *K*α radiation (λ = 1.5406 Å) at room temperature. The transmission electron microscope (TEM) measurement of the samples was explored using a Hitachi S-4800 field emission scanning electron microscope operating at 15 kV and a JEOL model JEM-F200 transmission electron microscope with an acceleration voltage of 200 kV. X-ray photoelectron spectra (XPS) were acquired using a VG ESCALAB MK II spectrometer with a monochromatic Mg *K*α source (1253.6 eV). Nitrogen and CO_2 adsorption/desorption measurements were carried out on a Tristar II 3020 surface area and porosity analyzer (Micromeritics). The specific surface area was calculated using the Brunauer–Emmett–Teller (BET) method. Room temperature UV/Vis diffuse reflectance spectra (DRS) were recorded on a Shimadzu UV–2550 UV/Vis spectrophotometer using $BaSO_4$ as the reference. Photoluminescence (PL) spectra of the photocatalysts were recorded on a LS55 Perkin–Elmer fluorescence spectrophotometer. PL lifetimes were determined using a single photon counting spectrometer with a microsecond pulse lamp as the excitation source (350 nm). Time-resolved photoluminescence (TRPL) spectra were also recorded by a transient fluorescence spectrometer (HORIBA Nanolog) equipped with a low temperature thermostatic tank as a sample pool in air and in vacuum, by using the excitation wavelength of 365 nm. Electron paramagnetic resonance (EPR) was tested using a Bruker EMX plus model spectrometer operated at room temperature. CO_2/CO temperature-programmed desorption (CO_2/CO–TPD) was obtained on a PX200 series multi-purpose adsorption instrument. Inductively coupled plasma-atomic Omission spectrometry (ICP–OES) was calculated using the PerkinElmer Optima 7000DV, all samples to be tested were dissolved in HF solution.

Photoelectrochemical measurements

Photoelectrochemical measurements were performed on a electrochemical workstation system (Princeton Versa STAT) with a conventional three-electrode cell. A Pt plate and a Ag/AgCl electrode were used as the counter and reference electrode, respectively.

The working electrodes were each prepared by coating a fluorine-doped tin oxide (FTO, 1.0 × 1.0 cm^2) substrate with an as-prepared sample, followed by drying in an oven. A 0.5 M Na_2SO_4 aqueous solution (purged with N_2 for 1 h) was used as the electrolyte. The light source was a 300 W Xe lamp. Transient photocurrent responses and EIS were recorded under intermittent visible-light irradiation. Mott–Schottky plots at the frequencies of 500, 800 and 1000 Hz were obtained using the three-electrode cell with saturated 0.5 M Na_2SO_4 as the electrolyte. Applied potential (E) with respect to NHE was calculated using the following equation: $E_{NHE} = E_{Ag/AgCl} + 0.197$.

Photocatalytic experiments

The photocatalytic CO_2 reduction activity was tested in a gas-solid reactor and the reduction gas phase product was measured out in a CEL-PAEM-D8-Plus closed circulation system (China Education Au Light, Beijing). 5 mg catalyst was dispersed into 1 mL ethanol and then the dispersion was spin-dropped uniformly onto a home-made quartz watch glass. After heating at 60 °C for several min, a thin film was prepared onto the watch glass homogeneously and placed on a triangle glass rack at the upper layer of a reactor, adding 10 mL water without any other extra photosensitizer or sacrificial reagent. A 300 W Xenon lamp (China Education Au Light, Beijing) was employed as the light source. Before irradiation, the reactor was vacuumed and was subsequently back filled with 20 mL ultra-pure CO_2 (99.999%), maintained for 30 min to a CO_2 adsorption and desorption equilibrium. The photocatalytic reactor was connected to an online gas chromatograph for hourly gas collection and analysis. The gas products were analyzed by a gas chromatograph (GC 7920-TF2A, China Education Au Light, Beijing) equipped with a flame ionization detector (FID) and a thermal conductivity detector (TCD). The quantification of all gases was performed based on calibration curves established using the corresponding standard gases. Chromatographic Standard Curves for Gas Detection: Standard curves for each product were established by manually injecting standard gases (CO and CH_4) in volumes of 1, 3, 5, 7, and 9 μL into the system three times. The average peak area from these three injections was utilized to construct the standard curves.

The product selectivity for CO_2 reduction to CO has been calculated using the following equation: Product selectivity of CO (%) = [n(CO)] / [n(CO) + n(CH_4)] × 100%, where n(CO) and n(CH_4) are the amounts of produced CO and CH_4.

The following control experiments were performed alongside the photocatalytic test: (1) without a light source, (2) without the photocatalyst, (3) without water, and (4) with high-purity Ar replacing CO_2. No photocatalytic products were detectable in any of these control experiments. Control experiments were essential to rule out any background contribution from the experimental system, solvent, or catalyst. The above tests confirm that the products unequivocally originated from CO_2 photoreduction, and not from carbon-based impurities in this system.

The photocatalytic water splitting performance was tested under solid-liquid reaction conditions. An on-line photocatalytic activity evaluation system (μGAS1000, Beijing Perfectlight) was used, which was connected with an on-line gas chromatograph (GC456i, Scion, Tcchcomp), argon as carrier gas. The photocatalytic overall water splitting performance was evaluated by dispersing 5 mg of photocatalyst in 30 mL of distilled water. No sacrificial agents or co-catalysts were added. Prior to the reaction, the reaction system was evacuated to remove air from the reaction system and dissolved air from the water. The irradiation was carried out using a 300 W Xenon lamp.

Determination of H_2O_2 concentration

The production of H_2O_2 was analyzed by the iodometry. 1 mL 0.1 mol L^{-1} potassium hydrogen phthalate ($C_8H_5KO_4$) aqueous solution and 1 mL 0.4 mol L^{-1} potassium iodide (KI) aqueous solution was added into the H_2O_2, which was hold for 30 min. The H_2O_2 molecules react with iodide anions under acidic condition to give triiodide anions which show a strong adsorption at around 350 nm. The concentration of triiodide anion was detected by UV-vis spectroscopy. A standard solution was prepared by diluting hydrogen peroxide 500-fold. Subsequently, aliquots of 6, 7, 8, and 10 μL of this diluted solution were taken to establish the calibration curve for estimating the the quantity of produced H_2O_2.

In situ diffuse reflectance infrared Fourier transform spectroscopy

In-situ diffuse reflectance infrared Fourier transform spectroscopy (DRIFTS) was measured by a Thermo Scientific iS50 FTIR spectrometer, with 64 scans accumulated at a resolution of 8 cm^{-1}. Prior to the measurement, the samples were flushed with Ar with a gas-flow rate of 30 $mL \cdot min^{-1}$ for 30 min. Then, the cell needs to be under conditions containing distilled water and then vacuumed to remove the gas. Besides, 1 MPa of CO_2 was introduced into the cell with a gas flow rate of 30 mL min^{-1} for 30 min and stabilized. Then, it was recorded and saved as background spectrum. After 30 min dark adsorption, turned on the lamp for illumination. At last, the DRIFTS of samples under irradiation were recorded for 60 min.

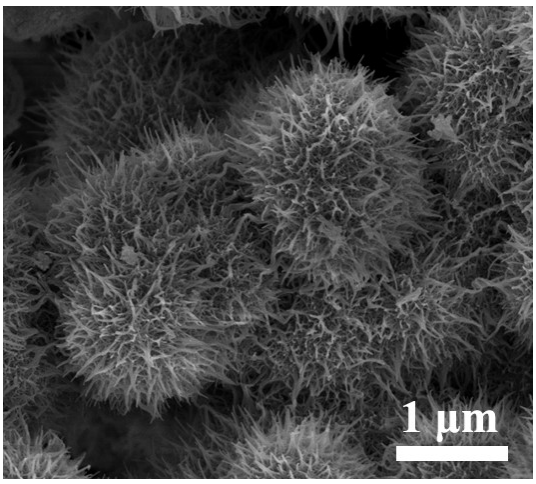

Fig. S1. SEM of the NbO precursor.

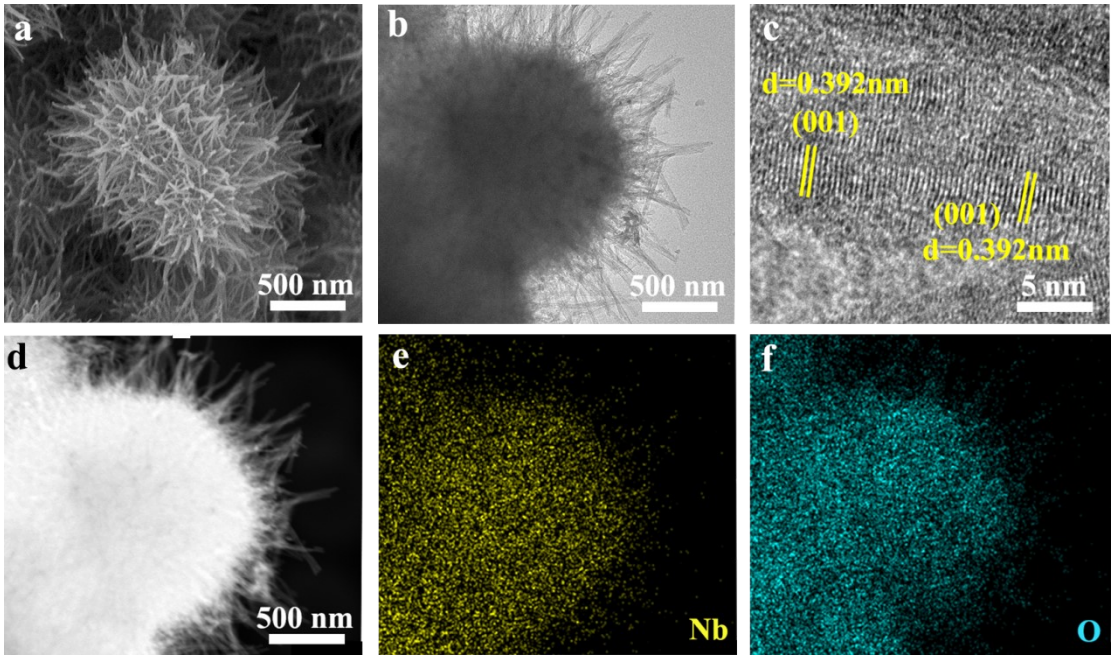

Fig. S2. (a) SEM, (b) TEM, and (c) HRTEM images, (d) STEM image and the corresponding EDX elemental mappings of (e) Nb and (e) O for Nb_2O_{5-x}.

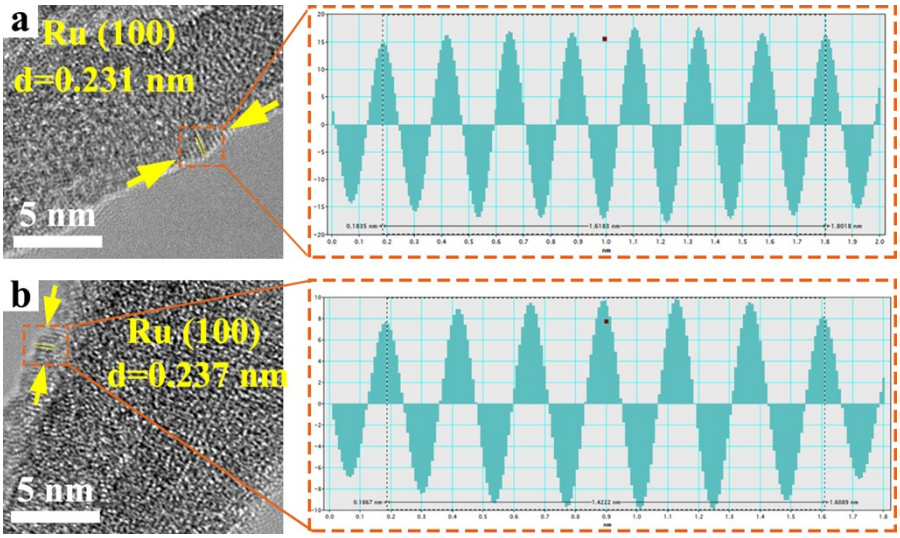

Fig. S3. (a, b) HRTEM images and the corresponding lattice fringes of Ru-Nb_2O_{5-x} in different regions.

Notably, lattice fringes with an interplanar spacing of 0.231 and 0.237 nm were observed on the outer surface of the nanothorns in Ru–Nb_2O_{5-x}, which can be attributed to the (100) plane of metallic Ru, confirming the presence of Ru^0 species.

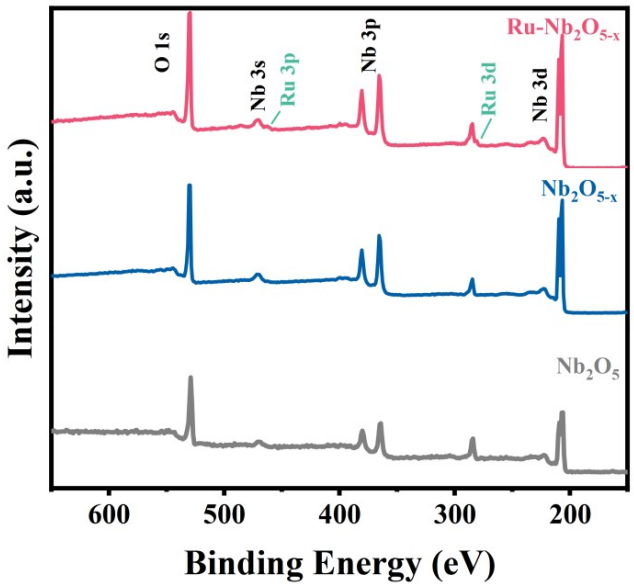

Fig. S4. XPS survey spectra of the Ru-Nb_2O_{5-x}, Nb_2O_{5-x} and Nb_2O_5.

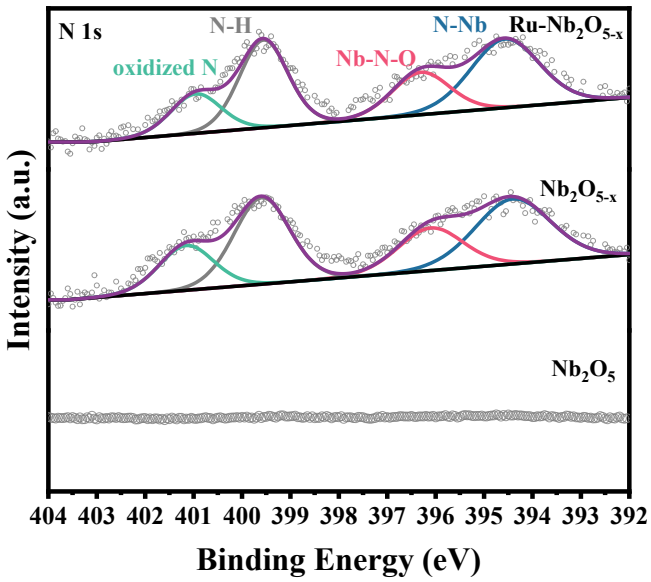

Fig. S5. High-resolution XPS spectra of N 1s for Ru-Nb_2O_{5-x}, Nb_2O_{5-x} and Nb_2O_5.

As shown in Fig. S5, the N 1s spectra can be deconvoluted into four signals at 394.41, 396.33, 399.56, and 400.94 eV, corresponding to N–Nb (substitutional N-doping), Nb–N–O (interstitial N-doping), N–H, and oxidized N, respectively.

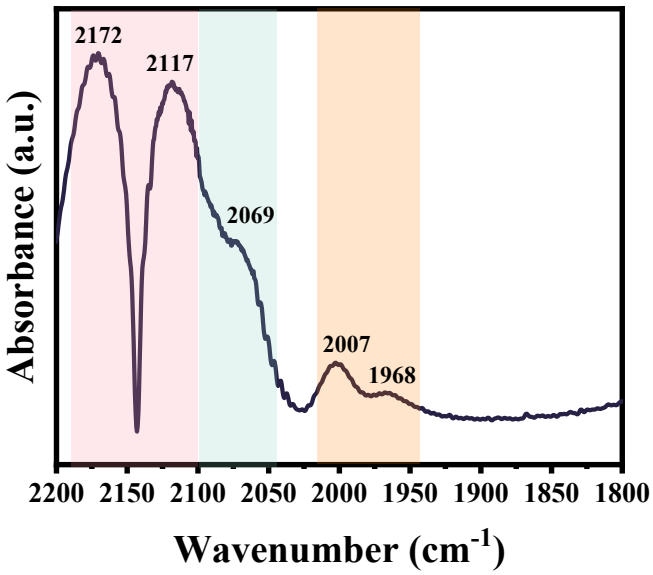

Fig. S6. CO-DRIFTS for the Ru-Nb_2O_{5-x}.

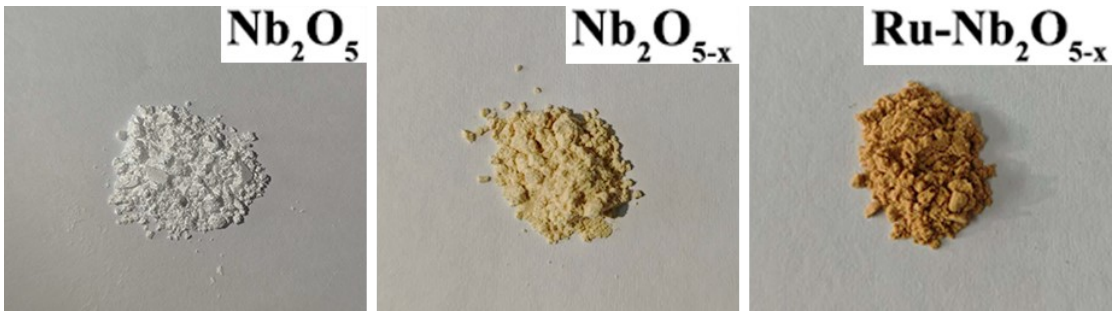

Fig. S7. The sample color of Nb_2O_5 (white), Nb_2O_{5-x} (yellow) and Ru-Nb_2O_{5-x} (brown).

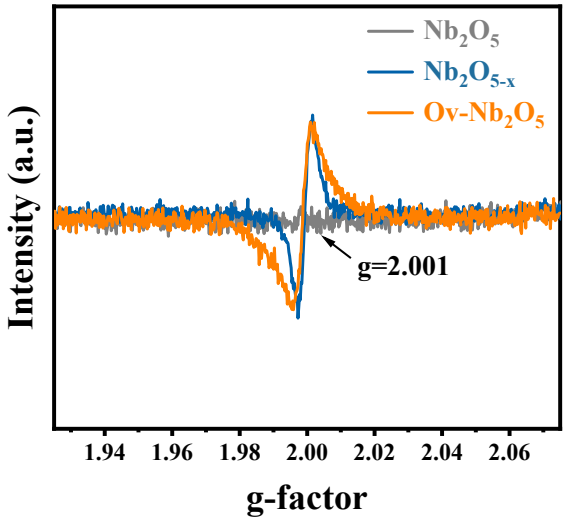

Fig. S8. EPR spectra of Nb_2O_5, Nb_2O_{5-x} and Ov-Nb_2O_5.

To explore the individual roles of N-doping and O_V, a reference sample Nb_2O_5 that contains only Ov without N species (denoted as Ov-Nb_2O_5) was synthesized using citric acid instead of arginine as the precursor, thereby excluding the nitrogen source. Initially, EPR spectroscopy was employed to confirm the presence and evaluate the concentration of O_V in the sample. As shown in Fig. S8, both Ov-Nb_2O_5 and Nb_2O_{5-x} exhibit a characteristic EPR signal at a g value of 2.001, which is attributed to unpaired electrons associated with Ov. Moreover, the comparable signal intensities indicate that both samples possess a similar concentration of Ov.

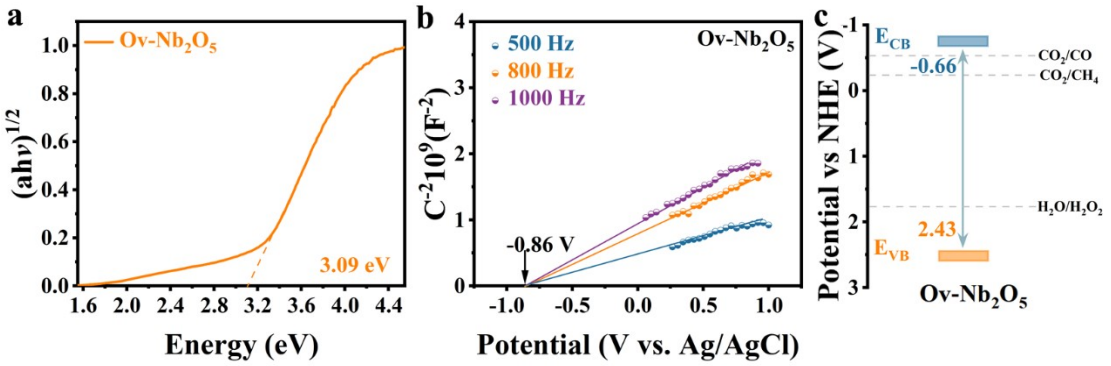

Fig. S9. (a) The Tauc plot, (b) Mott-Schottky plots and (c) Schematic energy band structure of Ov-Nb_2O_5.

UV-visible diffuse reflectance spectroscopy and Mott-Schottky tests were further carried out to determine the band structure. As shown in Fig. S9a, the corresponding bandgap energy of Ov-Nb_2O_5 are 3.09 eV, respectively. The slightly narrower bandgap of Ov-Nb_2O_5 compared with Nb_2O_5 (3.17 eV) indicates that Ov contributes to bandgap narrowing, whereas its larger bandgap relative to Nb_2O_{5-x} (2.88 eV) suggests that N-doping plays a crucial role in further modulating the electronic structure. Based on the flat band potential of Ov-Nb_2O_5 measured to be −0.86 V vs. Ag/AgCl (Fig. S9b), the band alignment of Ov-Nb_2O_5 is depicted, with the conduction and valence band positions at −0.66 and +2.43 V, respectively (Fig. S9c). By comparison, it is evident that N-doping significantly affects the position of the valence band, likely due to N-doping creating new electronic states and modulating the local electronic environment, which results in an upward shift of the valence band maximum. In summary, the Ov and N-doping exert a synergistic effect on the electronic structure of Nb_2O_5, thereby effectively reforming the band structure.

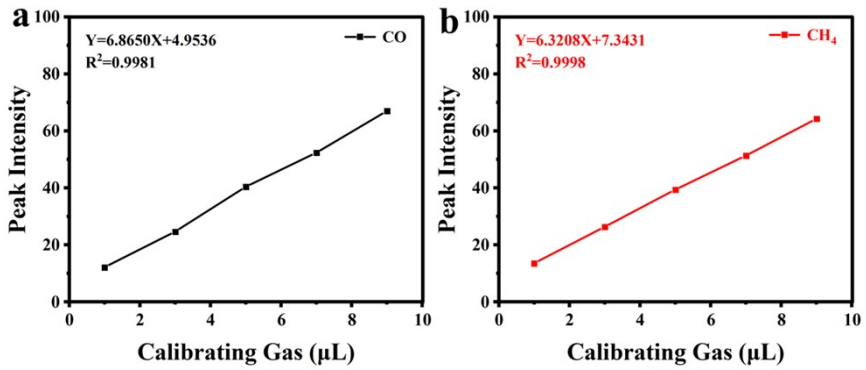

Fig. S10. Standard curves for CO (a) and CH_4 (b) on the FID detector**.**

The specific standard curves and their corresponding R^2 values are as shown in Fig. S10: X denotes the volume of the injected standard gas, while Y represents to the corresponding peak area.

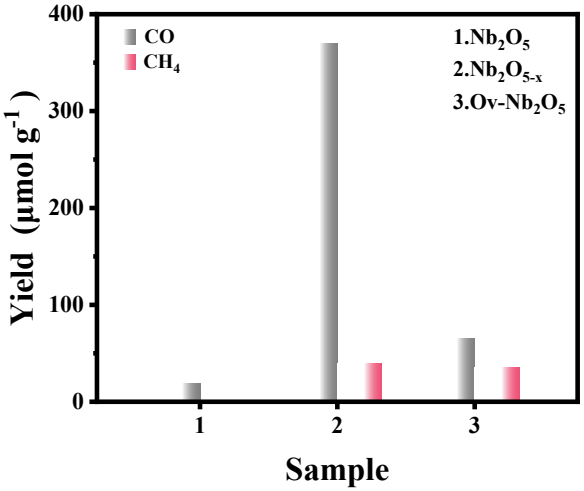

Fig. S11. The photocatalytic CO_2 reduction activities of Nb_2O_5, Nb_2O_{5-x} and Ov-Nb_2O_5 during 4 h.

As shown in Fig. S11, after 4 h of illumination, CO is the only product detected over pristine Nb_2O_5 (18.8 μmol g^{-1}). While, Ov-Nb_2O_5 exhibits markedly enhanced activity, producing 65.2 μmol g^{-1} of CO and 35.2 μmol g^{-1} of CH_4. The CO yield over Ov-Nb_2O_5 is 3.5 times higher than that of pristine Nb_2O_5, which can be entirely attributed to the contribution of Ov. In sharp contrast, the Nb_2O_{5-x} sample shows significantly enhanced CO_2 reduction performance, which mainly produced CO (369.4 μmol g^{-1}) ccompanied by a small amount of CH_4 (39.1 μmol g^{-1}). For Nb_2O_{5-x}, the CO yield is 5.7 times higher than that of Ov-Nb_2O_5, reflecting the significant effect of N-doping. Taken together, these results indicate that the enhanced CO_2 photoreduction performance of Nb_2O_{5-x} arises from the synergistic effect of Ov and N-doping, with the latter playing a key role in modulating the electronic structure.

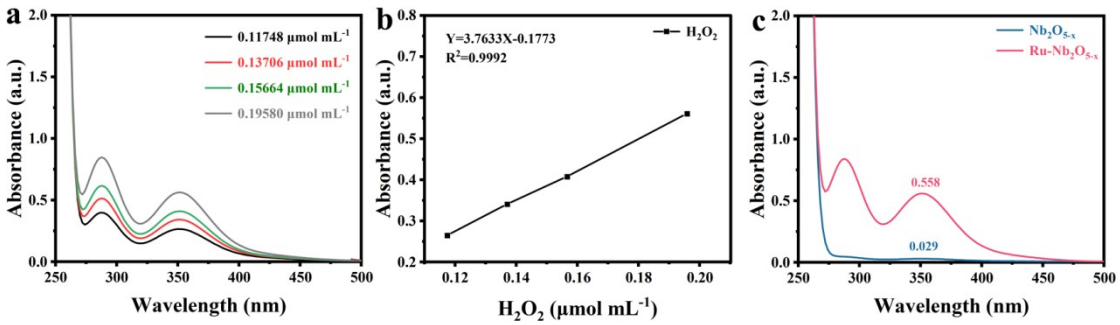

Fig. S12. (a-b) Standard curve for the measurement of H_2O_2 and (c) UV-vis spectra for detecting generated H_2O_2 over Nb_2O_{5-x} and Ru-Nb_2O_{5-x}.

As shown in Fig. S12, iodometric analysis of the hydrogen peroxide produced over Nb_2O_{5-x} and Ru-Nb_2O_{5-x} gave absorbance values of 0.558 and 0.029, respectively. According to the standard calibration curve, the corresponding H_2O_2 yields were calculated to be 1.582 and 0.444 μmol, respectively. The significantly higher yield obtained with Ru-Nb_2O_{5-x} corroborates that the incorporation of Ru species effectively promotes water oxidation.

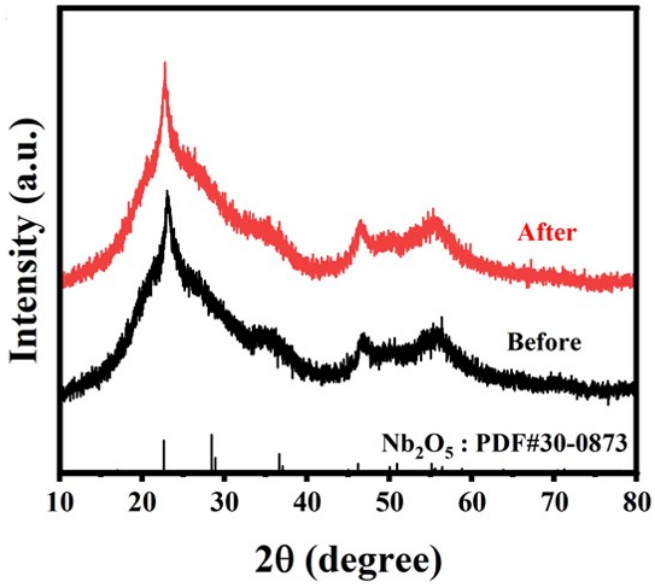

Fig. S13. XRD patterns of the Ru-Nb_2O_{5-x} before and after photocatalysis.

Fig. S14. SEM image of the Ru-Nb_2O_{5-x} after photocatalysis.

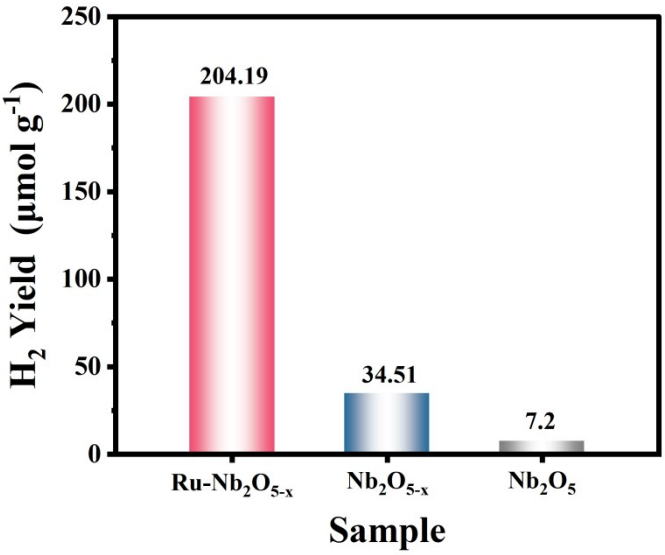

Fig. S15. The photocatalytic water splitting performance for Ru-Nb_2O_{5-x}, Nb_2O_{5-x} and Nb_2O_5.

The introduction of metallic Ru substantially improved the photocatalytic water-splitting efficiency, with Ru-Nb_2O_{5-x} achieving an H_2 evolution of 204.19 μmol g^{-1}, far surpassing that of Nb_2O_{5-x} (34.51 μmol g^{-1}). The result indicates that Ru is essential for facilitating the processes of water activation and dissociation.

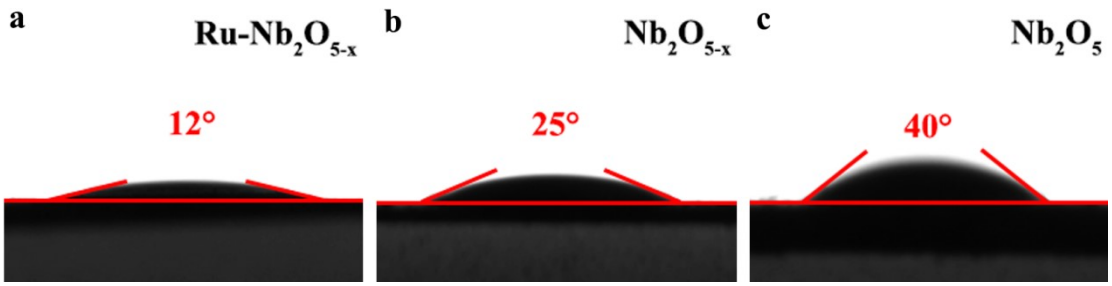

Fig. S16. Contact angle of (a) Ru-Nb_2O_{5-x}, (b) Nb_2O_{5-x} and (c) Nb_2O_5.

Table S1. Ru content in the different catalysts was determined by inductively coupled plasma optical emission spectrometry (ICP-OES).

Sample	Ru (mg L^{-1})	Ru content (wt%)
Ru-Nb_2O_{5-x}-1	0.167	0.33
Ru-Nb_2O_{5-x}-2	0.324	0.65
Ru-Nb_2O_{5-x}	0.512	1.02
Ru-Nb_2O_{5-x}-4	0.609	1.22

5 mg sample was digested with HF until a clear solution was obtained. The resulting solution was quantitatively transferred to a 100 mL volumetric flask, diluted to the mark, and homogenized by ultrasonication.

Table S2. Comparison of the reaction conditions and performances with other catalysts for photocatalytic CO_2 reduction.

Catalysts	Light source	Reaction condition	Products	Activity ($\mu mol\ g^{-1}\ h^{-1}$)	Reference
Ru-Nb_2O_{5-x}	300 W Xe lamp	Soild-gas	CO, CH_4	165.9	This work
Nb_2O_{5-x}	300 W Xe lamp	Soild-gas	CO, CH_4	92.4	This work
black Nb_2O_{5-x} NFs	300 W Xe lamp	Soild-liquid H_2O	CO, CH_4	10.59	1
V_O-Nb_2O_5 nanosheets	300 W Xe lamp	Soild-gas	CO, CH_4	4.30	2
Pd-Nb_2O_5 nanosheets	300 W Xe lamp	Soild-gas	CO, CH_4, C_2H_4, CH_3COOH	13.2	3
V_{Nb-O} NA	300 W Xe lamp	Soild-liquid H_2O	CO	43.9	4
Ag-20@Nb_2O_{5-x}	300 W Xe lamp (420 nm cut filter)	Soild-liquid H_2O+$NaHCO_3$+ $Ru(bpy)_3^{2+}$+ ascorbic acid	CO, CH_4	5.913	5
NB@CN (1:5)	5 W white LED light	Soild-liquid H_2O+$NaHCO_3$+ $Ru(bpy)_3^{2+}$+ ascorbic acid	CO, CH_4	0.155	6
$V_{O,N}$-NBCN	300 W Xe lamp (420 nm cut filter)	Soild-liquid H_2O+TEOA	CO, CH_4	0.89	7
$Nb_2O_5/W_{18}O_{49}$	300 W Xe lamp	Soild-gas	CO	40.15	8
Nb_2O_5-0.5%Cu	300 W Xe lamp	Soild-liquid H_2O	CO, CH_4	2.84	9
HBNO	300 W Xe lamp	Soild-gas	CO, CH_4	5.28	10
Nb-BBN120	300 W Xe lamp	Soild-gas	CO, C_2H_4	2.8	11
1ANbO	UV-light	Soild-gas	CO, CH_4	66.5	12
Bi_3TiNbO_9 nanosheets with OVs	300 W Xe lamp	Soild-gas	CO	20.91	13

Oxygen-vacancies tuned Bi_2MoO_6	**300 W Xe lamp**	**Soild-gas**	**CO**	**1.7**	**14**
WO_3–C-OV	**300 W Xe lamp (AM 1.5G filter)**	**Soild-gas**	**CO, CH_4**	**23.2**	**15**
Oxygen-vacancies tuned $BiOIO_3$ single crystals	**300 W Xe lamp**	**Soild-gas**	**CO**	**17.33**	**16**
Co single atoms/ oxygen-doped boron nitride	**300 W Xe lamp**	**Soild-liquid H_2O+TEOA**	**CO**	**32**	**17**
Vo-R $Bi_{24}O_{31}Br_{10}$ nanosheets	**300 W Xe lamp**	**Soild-liquid H_2O**	**CO**	**14.8**	**18**
BiOBr-1	**300 W Xe lamp**	**Soild-gas**	**CO, CH_4**	**71.23**	**19**
Ag/BiOCl-OV NFs	**300 W Xe lamp**	**Soild-gas**	**CO, CH_4**	**76**	**20**
Sur-Vo-BWO	**300 W Xe lamp**	**Soild-gas**	**CO, CH_4**	**18.73**	**21**
$BiO_{1-x}Cl$− OH	**300 W Xe lamp**	**Soild-liquid H_2O+$CoCl_2$**	**CO, CH_4**	**1.8**	**22**
BIO-LOV2	**300 W Xe lamp**	**Soild-gas**	**CO, CH_4**	**17.33**	**23**
DUC PBOC-0.5	**300 W Xe lamp**	**Soild-gas**	**CO, CH_4**	**16.02**	**24**

1

Table S3. The possible reaction path for the catalytic system of Nb_2O_{5-x} and Ru-Nb_2O_{5-x} samples.

$CO_2 + e^- + H^+ \rightarrow COOH^*$	(1)
$COOH^* + e^- + H^+ \rightarrow CO^* + H_2O$	(2)
$CO^* \rightarrow CO\uparrow + *$ or $CO^* + e^- + H^+ \rightarrow CHO^*$	(3)
$CHO^* + e^- + H^+ \rightarrow CH_2O^*$	(4)
$CH_2O^* + e^- + H^+ \rightarrow CH_3O^*$	(5)
$CH_3O^* + e^- + H^+ \rightarrow CH_4\uparrow + O^*$	(6)

Reference

[1] Lin, X.; Xia, S. H.; Zhang, L.; Zhang, Y. Y.; Sun, S. M.; Chen, Y. H.; Chen, S.; Ding, B.; Yu, Ji. Y.; Yan, J. H. Fabrication of Flexible Mesoporous Black Nb_2O_5 Nanofiber Films for Visible-Light-Driven Photocatalytic CO_2 Reduction into CH_4. *Adv. Mater.* **2022**, 34, 2200756.

[2] Wu, J. C.; Zhu, J. C.; Fan, W. Y.; He, D. P.; Hu, Q. Y.; Zhu, S.; Yan, W. S.; Hu, J.; Zhu, J. F.; Chen, Q. X.; Jiao, X. C.; Xie, Y. Selective Photoreduction of CO_2 to CH_4 Triggered by Metal-Vacancy Pair Sites. *Nano Lett.* **2024**, 24, 696-702.

[3] Ding, J. Y.; Du, P. J.; Li, P. P.; Liu, W. X.; Xu, J. Q.; Yan, W. S.; Pan, Y.; Hu, J.; Zhu, J. F.; Chen, Q. X.; Jiao, X. C.; Xie, Y. Highly Active Photoreduction of Atmospheric-Concentration CO_2 into CH_3COOH over Palladium Particles on Nb_2O_5 Nanosheets. *Angew. Chem. Int. Ed.* **2025**, 64, e202414453.

[4] Di, J.; Chen, C.; Wu, Y.; Chen, H.; Xiong, J.; Long, R.; Li, S. Z.; Song, L.; Jiang, W.; Liu, Z. Asymmetric Electron Redistribution in Niobic-Oxygen Vacancy Associates to Tune Non-Covalent Interaction in CO_2 Photoreduction. *Adv. Mater*. **2024**, 36, 2401914.

[5] Jiang, J. W.; Wang, X. F.; Guo, H. Enhanced Interfacial Charge Transfer/Separation By LSPR-Induced Defective Semiconductor Toward High CO_2RR Performance. *Small.* **2023**, 19, 2301280.

[6] Wang, X. F, Jiang, J. W.; Wang, L. L.; Guo, H. Efficient Nb_2O_5@g-C_3N_4 heterostructures for enhanced photocatalytic CO_2 reduction with highly selective conversion to CH_4. *Inorg. Chem. Front.* **2024**, 11, 123.

[7] Jiang, J. W.; Wang, X. F.; Xu, Q. J.; Mei, Z. Y.; Duan, L. Y.; Guo, H. Understanding dual-vacancy heterojunction for boosting photocatalytic CO_2 reduction with highly selective conversion to CH_4. *Appl. Catal. B: Environ.* **2022**, 316, 121679.

[8] Wang, Y. X.; Tao, R.; Mu, Y. Q.; Piao, T. Y.; Li, J. L.; M, Y.; F, X. X.; Y, Q. Z. Enhanced solid-gas-phase carbon dioxide photoreduction efficiency through in-situ growth of $W_{18}O_{49}$ on one-dimensional Nb_2O_5 nanofibers for forming ell-connected S-scheme heterojunction. *Fuel.* **2025**, 386, 134287.

[9] Chen, J. L.; Wang, T.; Yang, Z. Q.; Gao, P. Cu-modified Nb_2O_5 photocatalysts for high performance of CO_2 reduction. *Mater. Res. Bull.* **2025**, 184, 113288.

[10] Su, F. Y.; Wang, Z. S.; Tian, M. Z.; Liu, K. C.; Xie, H. Q.; Tu, W. G.; Zhang, Y. Z.; Li, X.; Jin, X. L.; Kong, X. Y. Constructing a crystalline-amorphous hydrated niobium pentoxide homojunction for superior photocatalytic CO_2 reduction into CH_4 with high selectivity. *Sci. Technol.* **2023**, 13, 5048-5057.

[11] J´essica A, O.; Juliana A, T.; Renato V, G.; Caue, R.; Francisco G. E, N.; Luís A.M, R. Photocatalytic CO_2 reduction over Nb_2O_5/basic bismuth nitrate nanocomposites. *Mater*. *Res*. *Bull*. **2021**, 133, 111073.

[12] Zeng, M.; Wu, Y. T.; Wang, Y.; Zhang, Z. Z.; Fu, X. Z.; Dai, W. X. Silver nanoparticle-enhanced photocatalytic CO_2 reduction over Ag/Nb_2O_5 under UV-vis light irradiation. *Appl. Catal. A.* **2023**, 666, 119412.

[14] Yu, H. J.; Chen, F.; Li, X. W.; Huang, H. W.; Zhang, Q. Y.; Su, S. Q.; Wang, K. Y.; Mao, E. Y.; Mei, Bastian.; Mul, G. D.; Ma, T. Y.; Zhang, Y. H. Synergy of

ferroelectric polarization and oxygen vacancy to promote CO_2 photoreduction. *Nat. Commun.* **2021**, 12, 4594.
[14] Zhang, Y. Z.; Zhi, X.; Harmer, J. R.; Xu, H. L.; Davey, K.; Ran, J. R.; Qiao, S. Z. Facet-specific Active Surface Regulation of Bi_xMO_y (M= Mo, V, W) Nanosheets for Boosted Photocatalytic CO_2 reduction. *Angew. Chem. Int. Ed*. **2022**, 61, e202212355.
[15] Lei, B.; Cui, W.; Chen, P.; Chen, L. C.; Li, J. Y.; Dong, A. C-Doping Induced Oxygen-Vacancy in WO_3 Nanosheets for CO_2 Activation and photoreduction. *ACS Catal.* 2022, 12, 9670-9678.
[16] Chen, F.; Ma, Z. Y, Ye, L. Q.; Ma, T. Y.; Zhang, T. R.; Zhang, Y. H.; Huang, H. W. Macroscopic Spontaneous Polarization and Surface Oxygen Vacancies Collaboratively Boosting CO_2 Photoreduction on $BiOIO_3$ Single Crystals. *Adv. Mater*. **2020**, 32, 1908350.
[17] Liang, J. L.; Zhang, H. B.; Song, Q. Q.; Liu, Z. Y.; Xia, J.; Yan, B. H.; Meng, X. M.; Jiang, Z. F.; Lou, X. W.; Lee, C. S. Modulating Charge Separation of Oxygen-Doped Boron Nitride with Isolated Co Atoms for Enhancing CO_2-to-CO Photoreduction. *Adv. Mater*. **2024**, 36, 2303287.
[18] Li, J. W, Sun, X. R.; Duan, Y. Q.; Ma, J. J.; He, C. Z.; Li, S. J. Oxygen vacancy-engineered ultrathin $Bi_{24}O_{31}Br_{10}$ for visible light-driven CO_2 reduction with nearly 100% CO selectivity in pure water. *Chem. Eng. J.* **2023**, 473 145383.
[19] Xie, J.; Lu, Z. J.; Feng, Y.; Huang, J. G.; Hu, J. D.; Hao, A. Z.; Cao, Y. L. A small organic molecule strategy for remedying oxygen vacancies by bismuth defects in BiOBr nanosheet with excellent photocatalytic CO_2 reduction. *Nano Res*. **2024**, 17, 297-306.
[20] Wang, F.; Guo, J. C.; Han, L. H.; Shen, H. X.; Zhu, L. L.; Chen, S. Oxygen vacancy-engineered BiOCl nanoflake with silver decoration for enhanced photocatalytic CO_2 reduction at solid-gas interface. *Chem. Eng. J.* **2023**, 478, 147365.
[21] Liu, H. H.; Chen, Y. X.; Wang, W. T.; He, X. Y.; He, Z. X.; Li, L.; Zeng, S. Y.; Cao, R. G.; Zhang, G. Q. *In situ* solvothermal reduction engineering enables delicate control over surface-rich oxygen vacancies on Bi_2WO_6 for highly efficient photocatalytic CO_2 reduction. *EES Catal.* **2023**, 1, 495.
[22] Sun, H. Y.; Lin, H. L.; Jia, X. M.; Li, X. Y.; Li, S.; Jin, X.; Wang, Q. L., Chen, S. F.; Cao, J. Dual structure cobalt sites on surface hydroxyl and oxygen vacancy of BiOCl for cooperative CO_2 reduction and tetracycline oxidation. *Appl. Catal. B: Environ.* **2024**, 359, 124514.
[23] Chen, F.; Ma, Z. Y.; Ye, L. Q.; Ma, T. Y.; Zhang, T. R.; Zhang, Y. H.; Huang, H. W. Macroscopic Spontaneous Polarization and Surface Oxygen Vacancies Collaboratively Boosting CO_2 Photoreduction on $BiOIO_3$ Single Crystals. *Adv. Mater*. **2020**, 32, 1908350.
[24] Wang, B.; Zhang, W.; Liu, G. P.; Chen, H. L.; Weng, Y. X.; Li, H. M.; Chu, P. K.; Xia, J. X. Excited Electron-Rich $Bi_{(3-x)}^{+}$ Sites: A Quantum Well-Like Structure for Highly Promoted Selective Photocatalytic CO_2 Reduction Performance. *Adv. Funct. Mater*. **2022**, 32, 2202885.